

FR0 radio galaxy jets – I. linking jet dynamics and high-energy emission in LEDA 55267 and LEDA 58287

A. F. S. Cardoso,^{1*} R. C. Anjos,^{1,2,3,4,5}

¹PPG Cosmo, CCE, Universidade Federal do Espírito Santo, Av. Fernando Ferrari, 540, 29075–910 Vitória, ES, Brazil

²Departamento de Engenharias e Exatas, Universidade Federal do Paraná (UFPR), Pioneiro, 2153, 85950-000 Palotina, PR, Brazil

³Programa de Pós-Graduação em Física e Astronomia, Universidade Tecnológica Federal do Paraná, Curitiba, PR 80230-901, Brazil

⁴Programa de pós-graduação em Física, Universidade Estadual de Londrina (UEL), Rodovia Celso Garcia Cid Km 380, 86057-970 Londrina, PR, Brazil

⁵Programa de Pós-Graduação em Física Aplicada, Universidade Federal da Integração Latino-Americana, 85867-670, Foz do Iguaçu, PR, Brazil

Accepted XXX. Received YYY; in original form ZZZ

ABSTRACT

Fanaroff–Riley type 0 (FR0) radio galaxies host anomalously compact jets whose disruption mechanism and high-energy emission remain poorly understood. We combine three-dimensional relativistic hydrodynamical (RHD) simulations with broadband spectral energy distribution (SED) modeling from radio to TeV energies, focusing on LEDA 55267 and LEDA 58287. Our simulations show that recollimation shocks trigger hydrodynamical instabilities that drive turbulence and rapid deceleration, preventing the jets from propagating beyond a few tens of parsecs and reproducing the observed compact radio morphology. Leptonic SED models adequately describe the observed emission up to GeV energies, but when simulated CTAO observations are included, statistical model comparison indicates strong evidence in favor of lepto-hadronic scenarios at TeV energies for both sources, a result that should be interpreted as a theoretical prediction to be tested by future observations. A leptonic analysis of the simulations reveals magnetized emitting regions with plasma beta parameters $\beta_p \sim 10^{-5}$ – 10^{-3} , orders of magnitude below values reported for extended FRI jets, consistent with jets retaining the magnetization inherited from the launching region and providing a natural physical link between the compact jet dynamics and the lepto-hadronic emission.

Key words: galaxies: jets – hydrodynamics – radiation mechanisms: non-thermal

1 INTRODUCTION

Supermassive black holes accreting matter give rise to what are known as active galactic nuclei (AGNs), which are capable of producing relativistic jets that can be collimated and extend up to megaparsec scales (Blandford et al. 2019). According to the unified model of AGNs (Urry & Padovani 1995), radio galaxies (RGs) are sources whose jets, characterized by strong radio emission, are not aligned with the line of sight, making them the dominant class of jetted AGNs. These sources are traditionally classified as Fanaroff–Riley type I (FRI) or Fanaroff–Riley type II (FRII) according to their radio morphology (Fanaroff & Riley 1974). FRI sources exhibit more diffuse and less powerful jets with edge-darkened structures, whereas FRII sources are more powerful and display edge-brightened morphologies with prominent hotspots. Within these jets, particles are accelerated to relativistic velocities, enabling electromagnetic interactions that can produce multimessenger particles, including neutrinos and ultra-high-energy cosmic rays (UHECRs) (see, e.g., Dermer et al. 2009; Collaboration et al. 2018; Tavecchio et al. 2018; Collaboration*† et al. 2022; Buson et al. 2022), as well as high-energy gamma-ray emission (see, e.g., Abdo et al. 2009, 2010; Inoue 2011; Di Mauro et al. 2014; Angioni et al. 2019; Stecker et al. 2019; Harvey et al. 2020; Rulten et al. 2020).

Although FRI and FRII radio galaxies have been extensively stud-

ied, a third class of radio galaxies, referred to as Fanaroff–Riley type 0 (FR0), was introduced to describe sources hosting anomalously compact jets that lack the extended radio structures characteristic of their classical counterparts (Ghisellini 2011; Baldi et al. 2015, 2018, 2019; Capetti et al. 2020b). Recent reviews have consolidated the current understanding of FR0 radio galaxies, highlighting their compact morphology, high core dominance, and lack of extended radio emission, despite sharing similar host and nuclear properties with FRIs (Baldi 2023). These properties indicate that FR0 jets undergo early disruption or inefficient propagation, making them key targets for studying the connection between jet dynamics and high-energy emission. According to the FROCAT catalog (Baldi et al. 2018), FR0s host black holes with masses in the range $10^{7.4}$ – $10^{9.0} M_\odot$ and are predominantly early-type, low-excitation galaxies found at redshifts $z < 0.05$. Remarkably, they are about five times more numerous than FRIs and approximately twenty times more numerous than FRIIs in the local Universe, making them the dominant population of jetted AGNs at low redshift. Given this abundance, FR0s may contribute significantly to the diffuse backgrounds of cosmic rays and neutrinos (Merten et al. 2021; Lundquist et al. 2025), making their characterization a problem of broad relevance to high-energy astrophysics. FR0s have 1.4 GHz radio luminosities in the range $10^{38.19}$ – $10^{40.27} \text{ erg s}^{-1}$ and share several properties with FRIs, such as their X-ray luminosity in the 2–10 keV band (Torresi et al. 2018). Despite these similarities, FR0 jets are confined to scales of less than 5 kpc, and no consensus explanation for this striking compactness

* E-mail: a.cardoso.fis@gmail.com

Table 1. Summary of the main properties of FR0, FRI, and FRII radio galaxies as reported in the FR0CAT, FRICAT, and FRIICAT catalogs (Baldi et al. 2018; Capetti et al. 2017a,b).

| Property | FR0CAT | FRICAT | FRIICAT |
|---------------------------------|---------------------------|---------------------------|---------------------------|
| Number | 108 | 219 | 122 |
| Redshift | $z < 0.05$ | $z < 0.15$ | $z < 0.15$ |
| L_r [erg s ⁻¹] | $10^{38.19} - 10^{40.27}$ | $10^{39.50} - 10^{41.30}$ | $10^{39.50} - 10^{42.50}$ |
| M_r | [-23, -21] | [-24, -21] | [-24, -20] |
| Jet size [kpc] | $r < 5$ | $r > 30$ | $r > 30$ |
| M_{BH} [M_{\odot}] | $10^{7.4} - 10^{9.0}$ | $10^{8.0} - 10^{9.5}$ | $10^{6.5} - 10^{9.5}$ |
| Host galaxy | Early-type | Early-type | Early-type |
| Excitation | Low | Low | High/Low |

has yet emerged. Among the proposed mechanisms, low black-hole spin, prograde accretion, and advection-dominated flows have been explored as possible causes for the suppression of jet growth (Garofalo et al. 2010; Garofalo & Singh 2019; Garofalo et al. 2024; Torresi et al. 2022). A summary of the main observational properties of the three classes is presented in Table 1, based on the FR0CAT, FRICAT, and FRIICAT catalogs (Baldi et al. 2018; Capetti et al. 2017a,b).

Other approaches to studying FR0 radio galaxies are based on the morphological analysis of their radio jets. These studies show that FR0s are extremely compact sources whose jets have moderately relativistic velocities and may undergo changes in direction, while also suggesting that these sources host low-luminosity AGNs capable of driving galactic winds (see, e.g., Baldi et al. 2019, 2025; Roy et al. 2021; Giovannini et al. 2023; Chilufya et al. 2024). A natural mechanism for suppressing jet propagation on kiloparsec scales is the development of recollimation shocks at the jet boundary, which can trigger hydrodynamical instabilities that promote turbulence, mixing with the ambient medium, and rapid deceleration of the flow. Complementary numerical investigations have explored this scenario in detail. Costa et al. (2024) and Costa et al. (2026) employ relativistic hydrodynamical (RHD) simulations to demonstrate how recollimation shocks can inhibit jet evolution on large scales. Building on these works, Boula et al. (2025) use simulations in the relativistic magnetohydrodynamics (RMHD) regime to investigate the role of the magnetic field in jet stability, also accounting for the presence of recollimation shocks. Lalakos et al. (2024) study jet formation by considering the black hole spin and, using general relativistic magnetohydrodynamics (GRMHD), propose that the infall of gas with negligible angular momentum onto rapidly rotating black holes prevents the formation of a stable accretion disc, rendering the jets intrinsically unstable. Meanwhile, Borodina et al. (2025) employ hydrodynamical (HD) simulations of low- and intermediate-power jets propagating through a turbulent interstellar medium (ISM), showing that such turbulence can suppress jet growth and evolution. Taken together, these recent studies indicate that FR0s play a relevant role in the physics of relativistic jets and may constitute promising environments for studying particle acceleration and the origin of UHECRs.

Although the jet power of FR0 radio galaxies is lower than that of FRI and FRII sources, this class of radio galaxies has been proposed as a promising source of neutrino emission (Tavecchio et al. 2018) and as a potential acceleration site of UHECRs (Merten et al. 2021; Lundquist et al. 2025). Indeed, very-high-energy gamma-ray emission has already been associated with FR0 jets. Grandi et al. (2016) associated gamma-ray sources from the 3FGL *Fermi*-LAT catalog (Acero et al. 2015) with the FR0 radio galaxy Tol 1326-379; however, no gamma-ray emission from this source was reported in the 4FGL *Fermi*-LAT catalog, and it therefore remains unclear

whether Tol 1326-379 is indeed a gamma-ray emitter (Fu et al. 2022). Pannikote et al. (2023) cross-matched the 4FGL *Fermi*-LAT catalog with radio and optical surveys and identified seven radio galaxies as candidate FR0 sources. More conclusively, Paliya (2021) reported GeV gamma-ray emission detected in the direction of two FR0 radio galaxies from the FR0CAT catalog, hereafter referred to as LEDA 55267 and LEDA 58287. These two sources are particularly well-suited for detailed investigation, as they are both located at low redshift ($z < 0.05$), exhibit parsec-scale jet-like radio structures confirmed by high-resolution VLBI observations (Giovannini et al. 2023), and display moderately relativistic jet velocities (Baldi et al. 2019) that make them amenable to RHD modeling. This detection opens a broad window for investigation, since FR0s are the most numerous jetted AGN population in the local Universe and may therefore represent a significant class of extragalactic gamma-ray sources detectable on Earth. More broadly, gamma-ray emission from low-power compact AGN has recently attracted increasing attention, with several works exploring particle acceleration and radiative processes in such systems (e.g., Cao et al. 2024; Bronzini et al. 2024a,b; Jiang et al. 2026). These studies indicate that even low-power jets may contribute significantly to the diffuse gamma-ray background, reinforcing the relevance of FR0 sources as potential high-energy emitters. Furthermore, Boughelilba & Reimer (2023, hereafter BR23) and Khatiya et al. (2024) explored the gamma-ray emission from LEDA 55267 and LEDA 58287 through spectral energy distribution (SED) modeling, considering lepto-hadronic and leptonic scenarios, respectively, reinforcing the idea that these sources are capable of accelerating particles to very high energies. Preliminary results combining RHD simulations with CTAO prospects (CTAO; Cherenkov Telescope Array Consortium et al. 2018) for these two sources were recently presented in Cardoso & Anjos (2026), and the present work provides a full account of those investigations.

The combination of compact, low-power jets and possible high-energy gamma-ray emission makes FR0 radio galaxies particularly intriguing, as it challenges the classical particle-acceleration scenarios associated with more powerful radio galaxies. A key difficulty in distinguishing between leptonic and lepto-hadronic emission models is that both scenarios produce degenerate predictions at GeV energies, while diverging significantly at TeV energies, where hadronic contributions become dominant. This makes next-generation Cherenkov observatories essential tools for breaking this degeneracy. In this work, we investigate LEDA 55267 and LEDA 58287 by combining two complementary approaches. On one hand, we exploit the most recent gamma-ray data from the 4FGL *Fermi*-LAT catalog (Abdollahi et al. 2020; Ballet et al. 2023) together with simulated observations from the Cherenkov Telescope Array Observatory (CTAO; Cherenkov Telescope Array Consortium et al. 2018) to model the broadband SEDs and evaluate the detectability of these sources at TeV energies. On the other hand, we present three-dimensional RHD simulations performed with the PLUTO code (Mignone et al. 2007) to reproduce the observed compact morphology of these sources. Crucially, the synthetic emission maps derived from the simulations serve as an independent consistency check for the emitting regions inferred from the SED analysis, linking jet dynamics directly to the observed radiative properties. We consider both leptonic and lepto-hadronic scenarios to constrain the physical parameters of both sources.

This paper is organized as follows. Section 2 presents the observational properties of LEDA 55267 and LEDA 58287 that motivate and constrain our modeling. Section 3 describes the methods adopted, covering the jet simulation setup, the SED modeling framework, and the CTAO observational configuration. Section 4 presents the re-

sults, including the jet dynamics and disruption, the synthetic emission maps, the broadband SED modeling under leptonic and lepto-hadronic scenarios, and the plasma magnetization analysis. Section 5 discusses the physical interpretation of the results and their broader implications for FRO jets as sites of high-energy particle acceleration and summarizes the main conclusions of this work.

2 SOURCES AND OBSERVATIONAL CONSTRAINTS

The radio galaxies LEDA 55267 and LEDA 58287 have been observed at multiple radio frequencies using the VLA, VLBA, VLBI, and EVN (Baldi et al. 2019; Giovannini et al. 2023). Both sources appear unresolved even at high angular resolution, confirming their extremely compact nature. LEDA 55267 exhibits a significant increase in flux density across epochs, suggesting variability, and on parsec scales presents a dominant core with a morphology consistent with a jet structure (Giovannini et al. 2023). LEDA 58287 similarly shows a slight increase in flux density and, on parsec scales, displays outer regions rotated with respect to the inner region, which is interpreted as evidence for the presence of a jet (Giovannini et al. 2023). The radio maps of both sources, observed with the EVN at 1.7 GHz and with the VLBA at 1.5 GHz for LEDA 55267 and LEDA 58287, respectively, are presented in Figure 1.

As shown in Figure 1, both sources display jet-like structures on scales of the order of tens of parsecs and have been detected in gamma-rays, making them well-suited targets for combined dynamical and radiative modeling. These observational constraints directly inform the setup of our jet simulations, which are designed to reproduce both the physical dimensions and the compact morphology observed at radio wavelengths.

3 METHODS

To investigate the physical properties of LEDA 55267 and LEDA 58287, we adopt three complementary methodological approaches that are closely coupled. First, we perform three-dimensional RHD simulations to reproduce the observed compact jet morphology and obtain the dynamical properties of the flow, including the thermal pressure distribution that will later be used to estimate the magnetic field strength. Second, we model the broadband SEDs of both sources from radio to gamma-ray energies, considering leptonic and lepto-hadronic particle populations, using the synthetic emission maps derived from the simulations for a consistency check on the physical extent of the emitting regions. Third, we simulate CTAO observations to assess the detectability of both sources at TeV energies, and to evaluate the diagnostic power of future observations in discriminating between emission scenarios. Each of these approaches is described in the following subsections.

3.1 Jet simulation setup

For the simulation of relativistic jets, we used the public PLUTO code (Mignone et al. 2007) in the RHD regime, performing a three-dimensional simulation in Cartesian coordinates. The HLLC Riemann solver and second-order Runge–Kutta (RK2) time stepping were employed in a computational domain with a grid of $350 \times 350 \times 1000$ cells, covering the physical domain $[-17.5, 17.5] \times [-17.5, 17.5] \times [2.5, 150]$ pc. Outflow boundary conditions were applied on all domain faces, with the exception of the lower z -boundary,

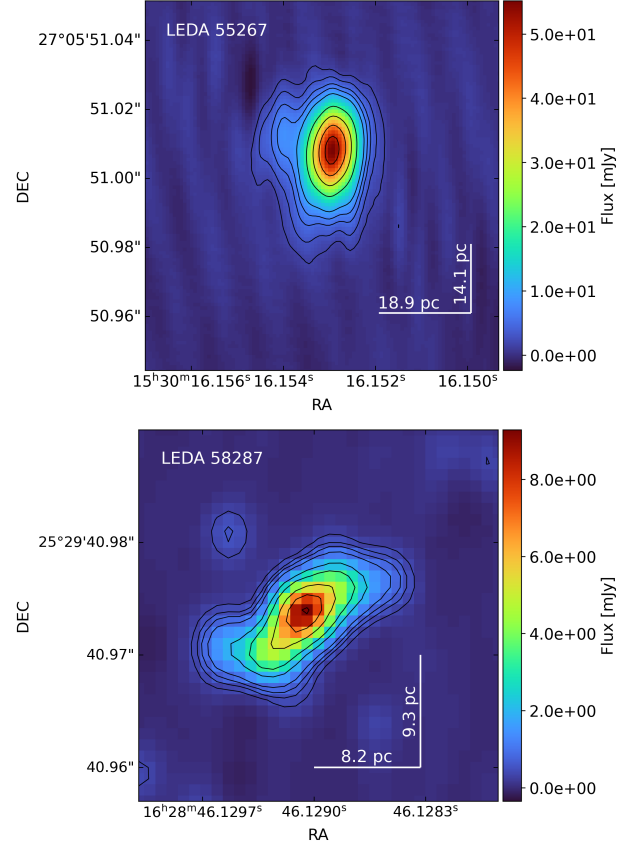


Figure 1. Radio maps of LEDA 55267 and LEDA 58287. The upper panel shows LEDA 55267 observed with the EVN at 1.7 GHz, with a peak flux density of $5.5 \times 10^{-2} \text{ Jy beam}^{-1}$ and contour levels of $(1.5, 3.0, 5.0, 7.0, 10.0, 20.0, 30.0, 40.0, 50.0) \times 10^{-3} \text{ Jy beam}^{-1}$. The lower panel shows LEDA 58287 observed with the VLBA at 1.5 GHz, with a peak flux density of $9.3 \times 10^{-3} \text{ Jy beam}^{-1}$ and contour levels of $(-0.3, 0.3, 0.5, 0.7, 1.0, 2.0, 3.0, 5.0, 7.0, 9.0) \times 10^{-3} \text{ Jy beam}^{-1}$. Both sources show compact morphologies consistent with jet structures on parsec scales. Radio maps adapted from Giovannini et al. (2023).

where the jet injection conditions are imposed. To track the jet material throughout the simulation, a passive scalar tracer field ϕ is advected alongside the fluid, initialized to $\phi = 1$ inside the jet cone and $\phi = 0$ in the external medium. This tracer allows us to distinguish jet material from the ambient medium at all times and to identify regions of mixing. The equations governing the RHD regime express the conservation of mass, momentum, and energy (Landau & Lifshitz 1959), given respectively by:

$$\frac{\partial D}{\partial t} + \nabla \cdot (D \mathbf{v}) = 0, \quad (1)$$

$$\frac{\partial \mathbf{M}}{\partial t} + \nabla \cdot (\mathbf{M} \otimes \mathbf{v} + p \mathbf{I}) = 0, \quad (2)$$

$$\frac{\partial E}{\partial t} + \nabla \cdot \mathbf{M} = 0, \quad (3)$$

where $D = \rho \Gamma$ is the rest-frame mass density, $\mathbf{M} = \rho h \Gamma^2 \mathbf{v}$ is the momentum density, and $E = \rho h \Gamma^2 - p$ is the total energy density. Here, ρ is the rest-mass density, Γ is the Lorentz factor, \mathbf{v} is the fluid velocity, p is the thermal pressure, and $h = 1 + e + p/\rho$ is the specific enthalpy, where e is the specific internal energy density.

For the equation of state (EOS), we adopt the Taub–Matthews (TM) EOS (Mignone et al. 2005), for which the specific enthalpy is given by:

$$h = \frac{5}{2}\Theta + \sqrt{\frac{9}{4}\Theta^2 + 1}, \quad (4)$$

where $\Theta = p/(\rho c^2)$, and we assume $c = 1$. Since FR0 jets are observed to be suppressed on kiloparsec scales, we base our simulation on the recollimation shock instability model proposed by Costa et al. (2024). In this framework, recollimation shocks trigger hydrodynamical instabilities that prevent the jet from further evolving, reproducing the compact morphology observed in FR0 sources. The jet is launched with an opening angle $\theta_j = 0.2$ rad, and at $t = 0$, within the conical region $(\sqrt{x^2 + y^2})/z < 0.2$, the jet velocity, density, and pressure are initialized according to

$$\mathbf{v} = \sqrt{1 - \frac{1}{\Gamma_j^2}} \frac{\mathbf{r}}{R}, \quad (5)$$

$$\rho_j(x, y, z, 0) = \rho_j(0, 0, z_0, 0) \left(\frac{R}{R_0}\right)^{-2}, \quad (6)$$

$$p_j(x, y, z, 0) = p_j(0, 0, z_0, 0) \left(\frac{R}{R_0}\right)^{-2\gamma}, \quad (7)$$

where z_0 is the jet launching distance, γ is the adiabatic index, and $R = \sqrt{x^2 + y^2 + z^2}$. In the region external to the jet, where $(\sqrt{x^2 + y^2})/z > 0.2$, the density and pressure of the ambient medium follow power-law profiles in z ,

$$\rho_{\text{ext}}(z, 0) = \rho_{\text{ext}}(z_0, 0) \left(\frac{z}{z_0}\right)^{-\eta}, \quad (8)$$

$$p_{\text{ext}}(z, 0) = p_{\text{ext}}(z_0, 0) \left(\frac{z}{z_0}\right)^{-\eta}, \quad (9)$$

where we adopt $\eta = 0.5$. As shown by Costa et al. (2024), the precise value of η does not critically affect the jet evolution, provided that $\eta < 2$. Since FR0 radio galaxies share several properties with FRIs, we adopt external medium pressure and density values comparable to those inferred for the FRI radio galaxy M87, namely $p_{\text{ext}} = 1.5 \times 10^{-9}$ dyne cm $^{-2}$ and $\rho_{\text{ext}} = 1.0$ cm $^{-3}$ (Sparks et al. 1996; Stawarz et al. 2006; Dainotti et al. 2012; Boizelle et al. 2025). We note that this choice represents an approximation, since the interstellar medium conditions in the host galaxies of LEDA 55267 and LEDA 58287 are not individually constrained by X-ray observations. However, these values are consistent with the range of thermal pressures reported for early-type galaxies at low redshift (see, e.g., Canizares et al. 1987; Boroson et al. 2011; Torresi et al. 2018), and Costa et al. (2024) show that the jet disruption behavior is not sensitive to moderate variations in the external medium parameters. Following Costa et al. (2024), we adopt a light jet with density $\rho_j = 10^{-4}$ cm $^{-3}$, well below that of the surrounding medium. The initial jet pressure is derived from the radio luminosity through the relation

$$L_j = \pi(z_0 \theta)^2 v_{j,z} \rho_{j,0} c^2 h_{j,0} \Gamma^2. \quad (10)$$

According to the FROCAT catalog (Baldi et al. 2018), the radio luminosities of LEDA 55267 and LEDA 58287 are $L_r = 10^{38.69}$ erg s $^{-1}$ and $L_r = 10^{39.15}$ erg s $^{-1}$, respectively. Since the two values differ by less than a factor of three and are of the same order of magnitude, we adopt the luminosity of LEDA 55267 as the reference to estimate the initial jet pressure, obtaining $p_j = 8.1 \times 10^{-8}$ dyne cm $^{-2}$

Table 2. RHD simulation setup parameters for the jet and external medium.

| Component | Quantity | Value | Units |
|-------------|----------------|-----------------------|-----------------|
| Jet | Density | 1.7×10^{-28} | g cm $^{-3}$ |
| | Velocity | $0.7 c$ | — |
| | Lorentz factor | 1.4 | — |
| | Pressure | 8.1×10^{-8} | dyne cm $^{-2}$ |
| | Opening angle | 0.2 | rad |
| | L_r | 4.9×10^{38} | erg s $^{-1}$ |
| Environment | Density | 1.7×10^{-24} | g cm $^{-3}$ |
| | Pressure | 1.5×10^{-9} | dyne cm $^{-2}$ |

from Equations 4 and 10. We verified that varying the jet pressure within this factor of three does not qualitatively alter the disruption dynamics described in Section 4.1. We adopt an initial jet velocity of $v_j = 0.7 c$, representative of the conditions close to the jet launching region. While VLBI observations and theoretical studies of FR0 radio galaxies indicate mildly relativistic bulk speeds on parsec scales ($\lesssim 0.5 c$; e.g. Baldi et al. 2015, 2019; Cheng & An 2018; Capetti et al. 2020a; Cheng et al. 2021; Giovannini et al. 2023), these measurements likely probe already decelerated flows rather than the pristine launch region. In our simulations, the jet undergoes rapid deceleration through recollimation shocks and hydrodynamical instabilities (Section 4.1), so that the bulk velocities recovered over most of the jet extent are fully consistent with the observational constraints. Adopting an initial velocity below $\sim 0.7 c$ would correspond to a less powerful jet with lower momentum flux, which would be even more easily disrupted by the same instabilities; in order for such a slower flow to evolve self-consistently with the same external medium, the ambient density would have to be reduced below the values inferred for early-type galaxy hosts, compromising the physical consistency of the setup. We note that the initial parameters of our simulation differ from those of Costa et al. (2024) in three main respects: we adopt $\Gamma = 1.4$ rather than $\Gamma = 10$, in agreement with the moderately relativistic speeds inferred for FR0 sources; the initial jet pressure is derived directly from the observed 1.4 GHz radio luminosity through Equation 10, rather than being imposed as a free numerical parameter; and the external medium properties are anchored to observationally motivated values for FRI hosts such as M87. The complete set of simulation parameters is summarized in Table 2.

3.2 SED modeling framework

To construct the broadband SEDs of LEDA 55267 and LEDA 58287, we compile multiwavelength data from radio to gamma-ray energies available in BR23, excluding the host galaxy contribution in order to isolate the non-thermal synchrotron and inverse Compton emission. These data are supplemented with the most recent flux measurements from the 4FGL *Fermi*-LAT catalog (Abdollahi et al. 2020; Ballet et al. 2023).

The particle populations responsible for the radio and gamma-ray emission are assumed to be co-spatial, consistent with the modeling framework of Khatiya et al. (2024). External radiation fields capable of driving significant particle–photon interactions are not expected for FR0 sources, since the internal synchrotron radiation field of the jet greatly exceeds any ambient external field. Nevertheless, we include the cosmic microwave background (CMB) as an additional seed photon field for inverse Compton scattering. The synchrotron self-Compton (SSC) emission is assumed to originate

in an effective emitting region located between 10^3 and 10^5 gravitational radii r_g from the central black hole, following the scenario proposed by [Khatiya et al. \(2024\)](#). This range corresponds to physical scales of the order of sub-parsec to tens of parsecs for the black hole masses typical of FRO sources ([Baldi et al. 2018](#)), consistent with the parsec-scale jet structures resolved by [Giovannini et al. \(2023\)](#) for both LEDA 55267 and LEDA 58287. This emitting region, therefore, represents an average parametrization of the physical conditions responsible for the observed non-thermal emission, grounded in the observational constraints available for both sources. Within this region, the spectral photon density of the synchrotron radiation field is given by

$$n_{\text{syn}}(E) = \frac{2.24}{4\pi R_{\text{jet}}^2 c} L_{\text{syn}}(E), \quad (11)$$

where E is the photon energy, R_{jet} is the radius of the emitting region, and $L_{\text{syn}}(E)$ is the synchrotron luminosity. The numerical factor 2.24 accounts for geometric effects under the assumption of a spherically symmetric emission region ([Atoyan & Aharonian 1996](#)).

The SEDs are fitted using the publicly available code NAIMA ([Zabalza 2015](#)), which implements analytical models for synchrotron and inverse Compton emission following [Aharonian et al. \(2010\)](#) and [Khanguyalyan et al. \(2014\)](#), respectively. The energy distributions of relativistic electrons and protons are modeled as an exponential cutoff power-law (ECPL) of the form

$$f_{e,p}(E) = A_{e,p} \left(\frac{E}{E_0}\right)^{-\alpha_{e,p}} \exp\left(-\frac{E}{E_{\text{cut},e,p}}\right), \quad (12)$$

where $A_{e,p}$ is the normalization at the reference energy E_0 , $\alpha_{e,p}$ is the spectral index, and $E_{\text{cut},e,p}$ is the cutoff energy for electrons and protons, respectively.

3.3 CTAO observational

To assess the detectability of LEDA 55267 and LEDA 58287 at TeV energies, we simulate CTAO observations using the one-dimensional (1D) ON/OFF observational technique implemented in the *Gammapy* software ([Donath et al. 2023](#); [Acero et al. 2025](#))¹. The ON region is defined as a circular aperture of radius 0.5° centered on each source, covering the GeV–TeV energy range of interest. Flux measurements from the 4FGL *Fermi*-LAT catalog ([Abdollahi et al. 2020](#); [Ballet et al. 2023](#)) are included to anchor the spectral models at GeV energies and ensure continuity across the full energy range covered by the simulation.

The annual visibility of both sources from the CTAO North and South sites was computed for 2026 at zenith angles of 20° , 40° , and 60° , and is listed in Table 3. Neither source is accessible from the CTAO South at zenith angles below 60° , whereas both sources accumulate between 556 and 580 hours of visibility per year from the CTAO North at all three zenith angles. We therefore adopt the CTAO North at a zenith angle of 20° as the reference observational configuration throughout this work.

The Instrument Response Functions (IRFs; [Observatory & Consortium 2021](#)) provided by the CTAO Consortium, optimized for an observation time of 50 hours, are used to generate the sensitivity curve. Detection is required to satisfy a minimum significance of 5σ with at least 10 detected photons, and a systematic background uncertainty of 0.05 is assumed throughout. An observation time of

Table 3. Annual visibility of LEDA 55267 and LEDA 58287 from the CTAO South and North arrays at zenith angles of 20° , 40° , and 60° . Dashes indicate configurations at which the source is not accessible.

| Source | CTAO array | Zenith angle | Visibility [h] |
|------------|------------|--------------|----------------|
| LEDA 55267 | South | 20° | — |
| | South | 40° | — |
| | South | 60° | 1190.50 |
| | North | 20° | 556.50 |
| | North | 40° | 561.50 |
| | North | 60° | 580.00 |
| LEDA 58287 | South | 20° | — |
| | South | 40° | — |
| | South | 60° | 1230.50 |
| | North | 20° | 560.00 |
| | North | 40° | 559.50 |
| | North | 60° | 574.00 |

200 hours is adopted for each source, from which we derive the CTAO sensitivity curve and the simulated gamma-ray flux points.

To account for gamma-ray attenuation by the Extragalactic Background Light (EBL), we apply the model of [Saldana-Lopez et al. \(2021\)](#). The EBL attenuates high-energy gamma-rays through pair production with intergalactic photons, with the effect increasing with source distance. This attenuation is incorporated into all spectral models to avoid overestimating the intrinsic source emission.

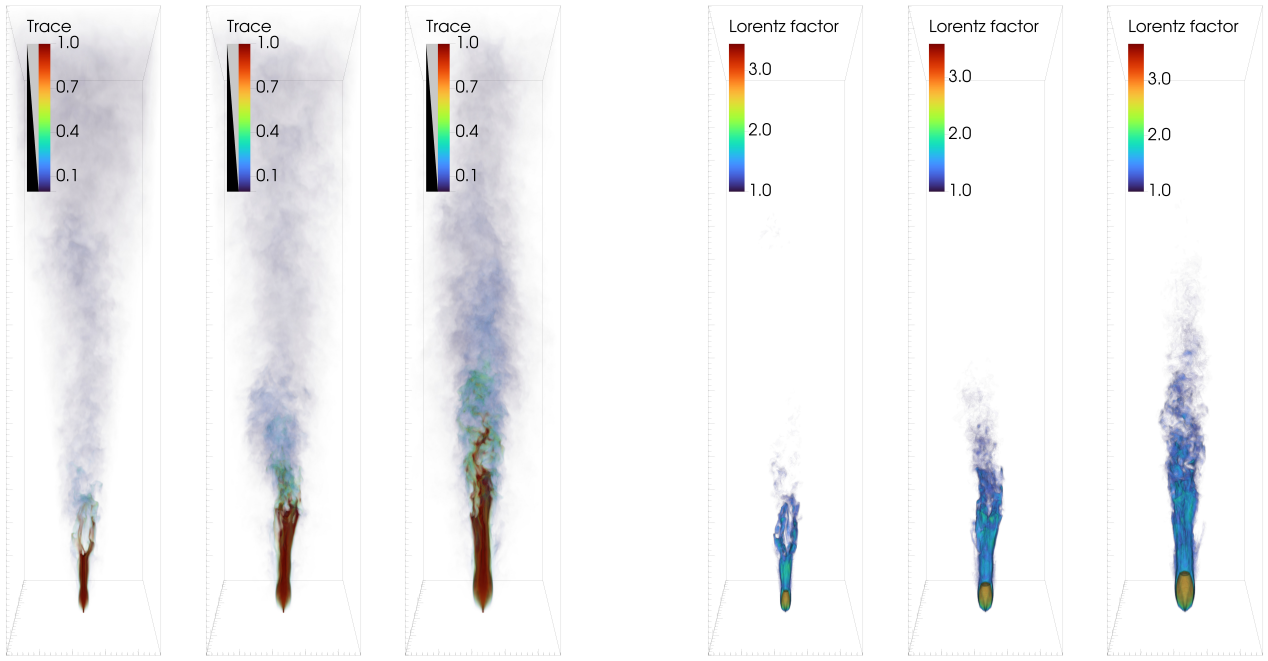
4 RESULTS

This section presents the results of our combined dynamical and radiative investigation of LEDA 55267 and LEDA 58287, organized to reflect the physical chain of reasoning that connects the three methodological approaches described in Section 3. We begin by presenting the jet dynamics and disruption mechanism emerging from the RHD simulations, followed by the synthetic synchrotron and inverse Compton emission maps that link the simulation results to the observed radio morphology. We then present the broadband SED modeling, incorporating the most recent *Fermi*-LAT data ([Abdollahi et al. 2020](#); [Ballet et al. 2023](#)) together with simulated CTAO observations at TeV energies, and assess the statistical preference between leptonic and lepto-hadronic scenarios through the Bayesian Information Criterion. Finally, we use the thermal pressures extracted from the simulations to estimate the plasma magnetization of the emitting regions through the β_p parameter, providing an independent consistency check between the hydrodynamical and radiative analyses. Taken together, these results build a coherent physical picture in which the compact morphology, the high-energy emission, and the magnetization state of FRO jets can be understood as manifestations of the same underlying jet dynamics.

4.1 Jet dynamics and disruption

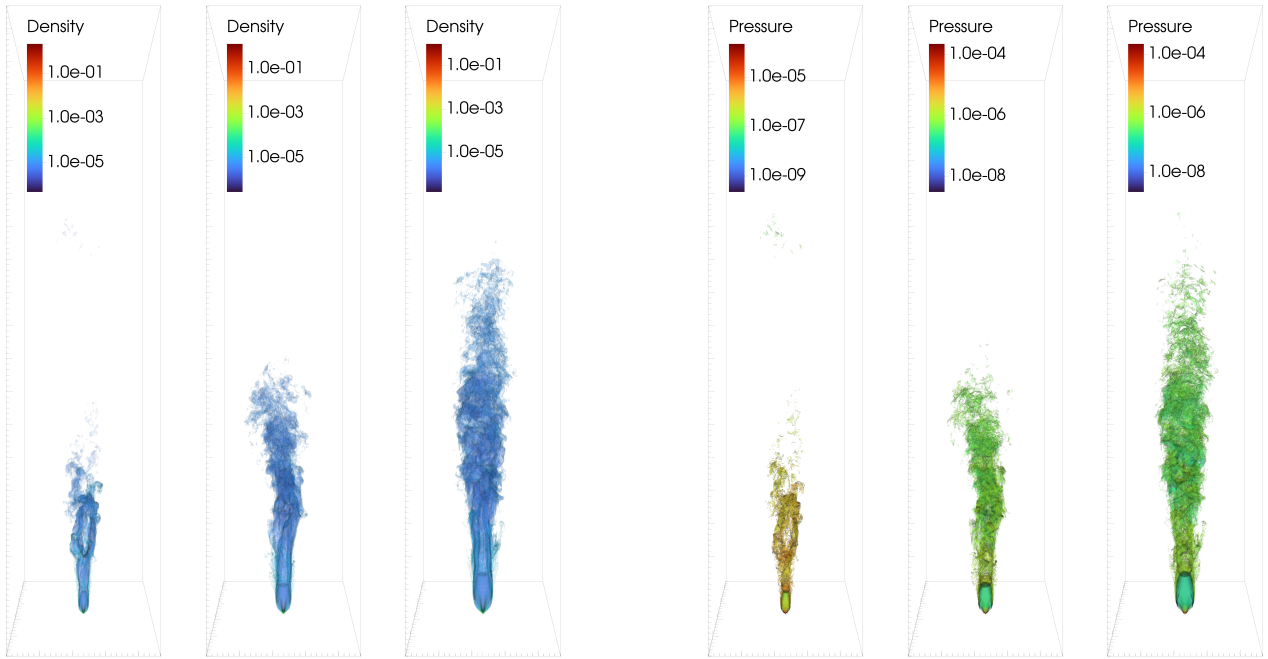
Figure 2 shows the simulated jet at three evolutionary times, 8.16 kyr, 24.48 kyr, and 40.79 kyr, illustrating the spatial distribution of the tracer fraction, Lorentz factor, rest-mass density, and thermal pressure. The simulation is initialized with the parameters listed in Table 2, chosen to reproduce the parsec-scale morphology and moderately relativistic velocities observed for LEDA 55267 and LEDA 58287 ([Baldi et al. 2019](#); [Giovannini et al. 2023](#)), following the recollimation shock instability framework of [Costa et al. \(2024\)](#).

¹ <https://gammapy.org>



(a) Tracer fraction, showing the spatial distribution of jet material throughout the simulation.

(b) Lorentz factor Γ , restricted to regions where the tracer fraction exceeds 10%.



(c) Rest-mass density ρ , normalized by $\rho_0 = 1.67 \times 10^{-24} \text{ g cm}^{-3}$, displayed where the tracer fraction exceeds 10%.

(d) Thermal pressure p , normalized by $p_0 = 1.50 \times 10^{-3} \text{ dyne cm}^{-2}$, within regions where the tracer fraction exceeds 10%.

Figure 2. RHD jet simulation snapshots at three evolutionary times: 8.16 kyr, 24.48 kyr, and 40.79 kyr (from left to right in each panel). Panels a–d show, respectively, the tracer fraction, Lorentz factor, density, and thermal pressure. The simulation is performed in a Cartesian domain (x, y, z) spanning $[-17.5, 17.5] \times [-17.5, 17.5] \times [2.5, 150]$ pc.

The tracer distribution in Figure 2a reveals that the jet material is rapidly disrupted as the flow evolves. At the earliest snapshot (8.16 kyr), the jet propagates in a relatively well-collimated manner within the first few parsecs, but already shows signs of lateral spreading and mixing at its head. By 24.48 kyr, the jet has lost its coherent columnar structure and the tracer is distributed across a broad, turbu-

lent volume, indicating that the jet has become heavily stratified. At 40.79 kyr, the tracer fills an even wider region and no clear jet boundary can be identified, confirming that the flow has been effectively disrupted well before reaching scales of several tens of parsecs. This behavior is consistent with the results of Costa et al. (2024) and Costa et al. (2026), who report qualitatively similar disruption in RHD sim-

ulations of light jets, and with [Borodina et al. \(2025\)](#), who show that jets propagating through a turbulent interstellar medium are similarly confined to compact scales.

The physical mechanism driving this disruption is visible in the sequence of panels. As soon as the jet begins to expand beyond the launching region, it becomes under-pressured relative to the external medium, triggering the formation of a recollimation shock. This shock breaks the jet axisymmetry and generates centrifugal instabilities at the jet–ambient medium interface, driving the flow into a highly turbulent regime. Subsequent recollimation events are suppressed by the growing instabilities, preventing any sustained re-acceleration of the flow.

The Lorentz factor maps in [Figure 2b](#) quantify the rapid deceleration that follows. At 8.16 kyr, relativistic velocities with $\Gamma \gtrsim 2$ are confined to the innermost few parsecs near the jet base. By 24.48 kyr, the high- Γ region has shrunk further and the bulk of the jet material is already sub-relativistic, with $\Gamma \sim 1$. At 40.79 kyr, essentially no relativistic motion is detectable beyond the immediate launch zone. This deceleration profile is broadly consistent with the moderately relativistic jet velocities inferred observationally for FRO sources ([Baldi et al. 2019](#); [Giovannini et al. 2023](#)) and with the kinematic constraints discussed by [Boula et al. \(2025\)](#) in the RMHD context.

The density maps in [Figure 2c](#) illustrate how the ambient medium is progressively entrained into the jet. At early times, the high-density external gas remains largely confined to the region surrounding the jet cone. As the instabilities develop, the density contrast between the jet and the ambient medium decreases substantially, reflecting efficient mass loading and mixing. By 40.79 kyr, the density distribution within the tracer-defined jet volume approaches that of the surrounding medium, signaling that the jet has been effectively decelerated and disrupted through momentum exchange with the environment. This mixing process is qualitatively similar to the entrainment reported by [Borodina et al. \(2025\)](#) for jets propagating through a clumpy ISM, and reinforces the picture in which jet disruption in FROs is driven primarily by interaction with the ambient medium rather than by intrinsic properties of the central engine alone.

The pressure evolution shown in [Figure 2d](#) completes this picture. At 8.16 kyr, the jet head maintains a pressure significantly above that of the surrounding medium, consistent with a ram-pressure dominated propagation phase. However, as the recollimation instabilities develop, the jet pressure drops sharply and approaches the ambient value of $p_{\text{ext}} = 1.5 \times 10^{-9}$ dyne cm $^{-2}$ throughout most of the flow volume. The pressure equilibration is essentially complete by 40.79 kyr, at which point the jet has lost its ability to drive further expansion. Taken together, the four panels of [Figure 2](#) consistently show that the simulated jet fails to propagate beyond a few tens of parsecs, in good agreement with the compact radio morphologies observed for LEDA 55267 and LEDA 58287 ([Giovannini et al. 2023](#)) and with the general picture of FRO jet confinement discussed in the recent literature ([Costa et al. 2024, 2026](#); [Boula et al. 2025](#); [Borodina et al. 2025](#)). The thermal pressures extracted from the simulated jet, particularly the values reached at late evolutionary times when the flow approaches pressure equilibrium with the ambient medium, will be used in [Section 4.4](#) to estimate the magnetic field strength via the plasma β_p parameter, independently of the SED fits, providing a consistency check between the dynamical and radiative analyses.

To complement the three-dimensional view shown above, azimuthally averaged characterization of the simulated jet, [Figure 3](#) shows the radial profiles of the Lorentz factor, density, and pressure at the same three evolutionary times. The profiles are obtained by averaging each quantity within cylindrical shells in the transverse plane, considering only regions where the tracer fraction exceeds

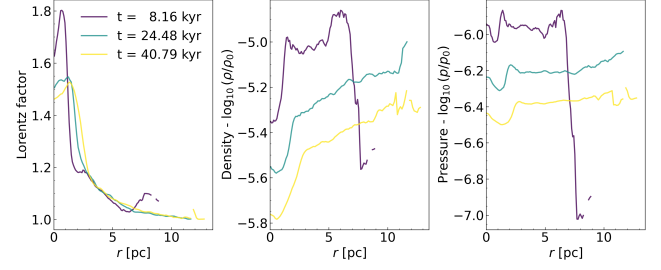


Figure 3. Azimuthally averaged radial profiles of the Lorentz factor (left), rest-mass density (middle), and thermal pressure (right) at three evolutionary times: $t = 8.16$ kyr, 24.48 kyr, and 40.79 kyr. Each profile is obtained by averaging the corresponding quantity over cylindrical shells in the plane transverse to the jet axis, restricted to cells where the tracer fraction exceeds 10%, thereby isolating the jet material from the ambient medium. The profiles illustrate the rapid radial decline of the Lorentz factor, the progressive density flattening driven by entrainment, and the tendency of the pressure profile to relax towards the external value as the jet evolves.

10%, so that they describe the jet material rather than the ambient medium. The Lorentz factor decreases sharply with radius at all epochs, confirming that relativistic velocities are confined to the innermost regions and rapidly become sub-relativistic elsewhere, in agreement with the spatial maps and consistent with the turbulent mixing scenario. The density profiles increase gradually with radius, reflecting the entrainment of ambient gas, an effect that becomes progressively more pronounced as time advances and is most evident at 40.79 kyr, in line with the diffuse structure visible in [Figure 2a](#) at this epoch. The pressure profiles flatten radially as the system evolves, approaching the external value at large radii, which signals the transition from a driven jet phase to a disturbed flow dominated by turbulence. Overall, the radial profiles reinforce the conclusions drawn from the three-dimensional maps regarding the rapid deceleration, efficient mixing, and early disruption of the flow.

4.2 Synthetic morphology and emission maps

To evaluate the morphology and structure of the simulated jets and compare them with the radio maps presented in [Figure 1](#), we produce synthetic maps of the synchrotron emission based on the jet simulations. These maps serve a dual purpose: they allow a direct morphological comparison with the observed radio structures, and they identify the regions of enhanced emissivity that will inform the SED modeling presented in [Section 4.3](#). The magnetic field in the simulated jet is assumed to be proportional to the thermal pressure, an approximation widely adopted in the literature when direct observational constraints on the field geometry are unavailable ([Gomez et al. 1995](#); [Nawaz et al. 2016](#)). The physical justification for this assumption and its implications for the magnetization of the emitting regions are discussed in [Section 4.4](#). Under this prescription, the synchrotron emissivity in the rest frame is computed following [Sutherland & Bicknell \(2007\)](#) as

$$j_\nu = \lambda p^{\alpha+3/2} \delta^{2+\alpha}, \quad (13)$$

where λ is a parameter that isolates the jet plasma from the ambient medium, p is the gas pressure assumed proportional to the total particle pressure, and the spectral index is fixed at $\alpha = 1.0$. The Doppler factor δ accounts for relativistic beaming effects and is computed locally in each cell as

$$\delta = \frac{1}{\Gamma(1 - \beta \cos \theta')}, \quad (14)$$

where β is the flow velocity in units of c , Γ is the Lorentz factor, and $\theta' = \cos^{-1}(v'_{\text{LOS}}/|v'|)$ is the angle between the rotated velocity vector \mathbf{v}' of each cell and the line-of-sight (LOS) direction, with v'_{LOS} being the LOS component of \mathbf{v}' (Nawaz et al. 2016). The synthetic emissivity along the line of sight is then obtained by integrating the rotated three-dimensional emissivity field as

$$I_\nu = \int j_\nu ds. \quad (15)$$

As discussed in Nawaz et al. (2016), the projected morphology of the observed source depends on both the inclination angle between the jet propagation axis and the line of sight, and the azimuthal viewing angle. For LEDA 55267, we project the emissivity integrated along the jet evolution axis z onto the (x, y) plane without applying any reorientation, corresponding to a configuration in which the simulated jet is approximately aligned with the line of sight, producing a compact, centrally concentrated emission pattern consistent with the unresolved radio morphology of LEDA 55267 (Giovannini et al. 2023). For LEDA 58287, we apply a three-dimensional reorientation to the simulated jet volume. Defining the z axis as the initial line of sight, the jet is rotated through two successive transformations: a rotation of $\theta = 15^\circ$ in the (y, z) plane around the x axis, which inclines the jet axis with respect to the plane of the sky, followed by a rotation of $\chi = 15^\circ$ in the (x, z) plane around the y axis, which adjusts the position angle of the jet in the two-dimensional projection. This produces a more asymmetric projected distribution of the synchrotron emission, in good agreement with the rotated outer structure observed in LEDA 58287 (Giovannini et al. 2023). The resulting synthetic synchrotron emission maps are presented in Figure 4.

The viewing angles adopted here are not uniquely determined and should be understood as effective geometrical configurations capable of reproducing the observed source morphologies, rather than as definitive measurements of the true jet orientations. This is consistent with the findings of Giovannini et al. (2023), who show that moderately relativistic FR0 jets are compatible with a wide range of inclination angles with respect to the line of sight. Furthermore, Masaro et al. (2020) showed that BL Lac objects inhabit environments statistically consistent with those of FR0 radio galaxies, suggesting that a fraction of BL Lacs may correspond to FR0 sources observed at small viewing angles. Within this broader orientation framework, the aligned configuration adopted for LEDA 55267 should be interpreted as a limiting case rather than as a definitive measurement of the jet inclination.

A grid-like pattern is visible at the base of the jet in Figure 4. This is a numerical artifact arising from the relatively small number of computational cells across the jet cross-section at the injection boundary, which prevents the base of the jet from appearing fully cylindrical in projection. The structure is therefore a resolution effect with no physical significance, and is expected to smooth out at higher numerical resolution. It does not affect the morphological features of the scales of interest, namely the overall extent and asymmetry of the projected emission distribution.

For completeness, we also produce synthetic maps of the inverse Compton emission at an energy of 3.0 GeV, using the same angular orientations as in Figure 4. These maps are computed with the publicly available code NAIMA² (Zabalza 2015), adopting a power-law electron energy distribution with an exponential cutoff whose spectral index and cutoff energy are taken from the leptonic fits described in Section 4.3. Particle acceleration is assumed to operate only in

² Additional information, including installation and implementation details, is available at <http://naima.readthedocs.org>.

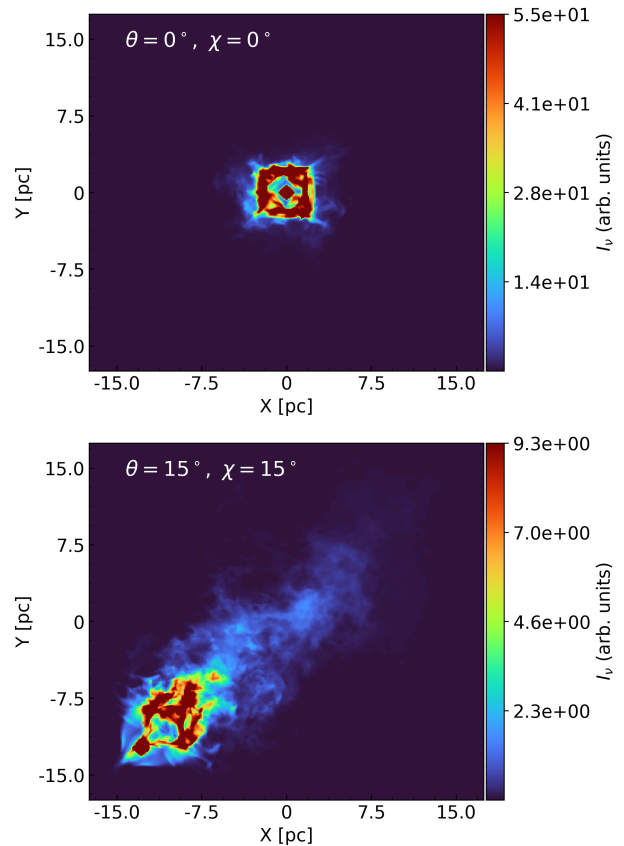


Figure 4. Synthetic synchrotron emission maps of the simulated jet projected onto the (x, y) plane. The upper panel represents LEDA 55267, obtained without jet reorientation ($\theta = 0^\circ$, $\chi = 0^\circ$), corresponding to a configuration approximately aligned with the line of sight. The lower panel represents LEDA 58287, obtained after rotating the jet by $\theta = 15^\circ$ around the x axis and $\chi = 15^\circ$ around the y axis, producing a more asymmetric projected morphology consistent with the observed radio structure. The color bar indicates the synchrotron intensity in arbitrary units.

regions where the local Mach number exceeds unity, with an electron acceleration efficiency $f_e = 0.5$. The resulting synthetic inverse Compton emission maps are presented in Figure 5.

Despite originating from distinct radiative mechanisms, the synthetic synchrotron and inverse Compton maps share similar morphological features. This is the expected outcome of our framework, since the inverse Compton emission is primarily driven by synchrotron self-Compton (SSC) processes arising from the same population of relativistic electrons responsible for the synchrotron radiation. In both cases, the emission is concentrated in the central region of the jet, where the tracer analysis of Section 4.1 identified the most active zones of jet–ambient medium interaction, associated with the recollimation shocks and turbulent mixing at the jet boundary. The co-spatiality of the maximum emission intensities does not simply reflect the radiative coupling between synchrotron and inverse Compton processes, but also underscores the role of these dynamical structures as common sites of particle acceleration. This result provides independent support for the assumption of co-spatial emitting populations adopted in the SED modeling of Section 4.3. The synthetic maps reproduce the main morphological features of the observed radio emission in Figure 1 reasonably well, lending physical credibility to the overall simulation setup.

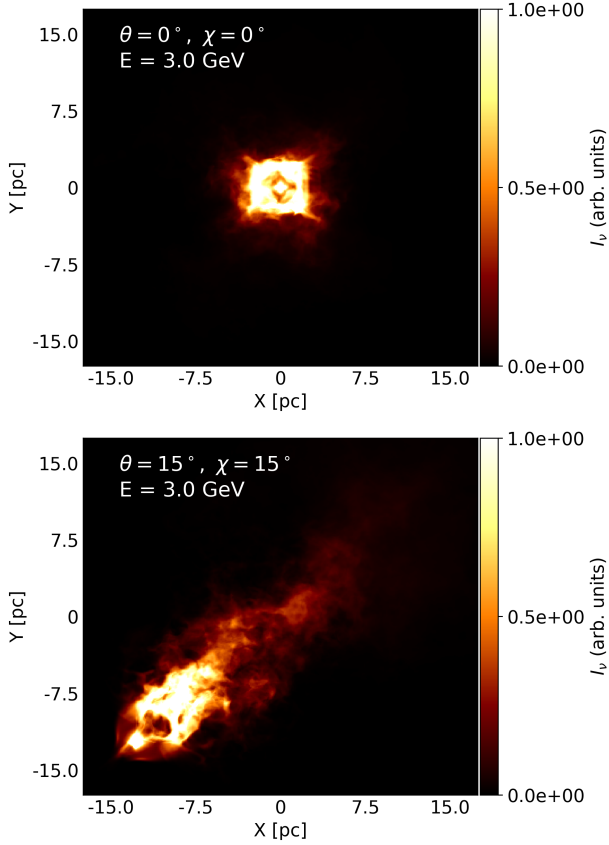


Figure 5. Synthetic inverse Compton emission maps of the simulated jet projected onto the (x, y) plane, computed at an energy of 3.0 GeV. The upper panel represents LEDA 55267, obtained without jet reorientation ($\theta = 0^\circ$, $\chi = 0^\circ$). The lower panel represents LEDA 58287, obtained after rotating the jet by $\theta = 15^\circ$ around the x axis and $\chi = 15^\circ$ around the y axis. Emission is restricted to regions where the local Mach number exceeds unity, for which an electron acceleration efficiency of $f_e = 0.5$ is assumed. The color bar indicates the inverse Compton intensity in arbitrary units.

4.3 Leptonic and lepto-hadronic modeling

In this section, we present the SED fitting results for LEDA 55267 and LEDA 58287. Their multi-wavelength luminosities, together with the corresponding telescopes/instruments, are summarized in Table 4. For the currently available flux data points, we consider only the leptonic scenario, following the approach of Khatiya et al. (2024). When the simulated CTAO flux points are included, we explore both leptonic and lepto-hadronic scenarios to assess whether a hadronic contribution may play a role in the production of the highest-energy gamma-ray emission. We stress from the outset, that the preference for the lepto-hadronic scenario discussed below is a theoretical prediction based on simulated CTAO observations, not a constraint imposed by currently available data. The simulated CTAO flux points are generated under the assumptions described in Section 3.3, namely a 200 hour observation with the CTAO North array at a zenith angle of 20° , using the spectral models fitted to the existing multiwavelength data as input and applying EBL attenuation following Saldana-Lopez et al. (2021). These points, therefore, represent the flux values that would be measured if the source emission followed the input spectral model, and their role is to extend the observational coverage into the TeV regime where leptonic and lepto-hadronic scenarios diverge.

Table 4. Representative multi-wavelength luminosities of LEDA 55267 and LEDA 58287, together with the telescopes/instruments from which the fluxes are taken.

| Band | Energy | Luminosity [erg s ⁻¹] | Telescope |
|-------------------|-----------|-----------------------------------|------------|
| <i>LEDA 55267</i> | | | |
| Radio | 1.4 GHz | 6.58×10^{38} | NVSS/FIRST |
| X-ray | 1.4 keV | 2.47×10^{41} | Swift |
| γ -ray | 5.5 GeV | 7.08×10^{41} | Fermi |
| γ -ray | 55 GeV | 4.18×10^{41} | Fermi |
| <i>LEDA 58287</i> | | | |
| Radio | 1.4 GHz | 1.25×10^{39} | NVSS/FIRST |
| X-ray | 0.5-7 keV | 1.49×10^{41} | Chandra |
| γ -ray | 5.5 GeV | 5.84×10^{41} | Fermi |
| γ -ray | 55 GeV | 4.64×10^{41} | Fermi |

The best-fit parameters obtained with NAIMA for each source and scenario are listed in Table 5.

For both sources, the leptonic best-fit parameters are in good agreement with those reported by Khatiya et al. (2024), with magnetic field strengths in the range 0.002–0.02 G, which are also consistent with the estimates of Merten et al. (2021). The small differences with respect to Khatiya et al. (2024) are attributable to the inclusion of the most recent 4FGL *Fermi*-LAT flux points (Abdollahi et al. 2020; Ballet et al. 2023). As visible in the top panels of Figure 6, the leptonic model reproduces the observed radio, X-ray, and GeV data satisfactorily. The synchrotron component peaks in the radio band, while the inverse Compton component, dominated by SSC emission, accounts for the GeV flux. The negligible contribution from CMB inverse Compton scattering is consistent with the compact nature of FRO jets, in which the internal synchrotron radiation field greatly exceeds any external seed photon field, as also noted by Khatiya et al. (2024) and Bougheliiba & Reimer (2023). The higher magnetic field strengths inferred here, when compared to those typically reported for extended FRI jets, follow naturally from the compact nature of FRO sources, since the SED is being modeled close to the emitting region, where the magnetic energy density inherited from the launching site has not yet been significantly dissipated.

However, the leptonic model alone does not constrain the TeV regime, since *Fermi*-LAT observations do not extend to these energies. The middle panels of Figure 6 show that, when the simulated CTAO flux points are included, the leptonic model struggles to reproduce the TeV emission simultaneously with the GeV data, requiring a harder electron spectrum and a significantly higher cutoff energy ($E_{\text{cut,e}} \sim 3$ TeV for LEDA 55267 and ~ 2 TeV for LEDA 58287) compared to the fits based on currently available data. This tension motivates the exploration of a lepto-hadronic scenario, in which relativistic protons interact with ambient photons or matter to produce additional high-energy emission through pion decay (Dermer et al. 2009; Tavecchio et al. 2018). In the lepto-hadronic fits shown in the bottom panels of Figure 6, the hadronic component rises steeply at TeV energies and accounts naturally for the simulated CTAO flux points, while the leptonic component continues to describe the radio and GeV data.

The hadronic model parameters listed in Table 5 deserve brief discussion in terms of their physical implications. The proton spectral indices $p_p = 0.01$ for both sources are unusually hard, suggesting that the proton energy distribution is nearly flat at injection, which may reflect an efficient diffusive shock acceleration at the recollimation

shocks identified in our RHD simulations (Blandford & Eichler 1987; Kowal et al. 2011). The proton cutoff energies $E_{\text{cut,p}} = 3.78$ TeV for LEDA 55267 and $E_{\text{cut,p}} = 2.86$ TeV for LEDA 58287 are consistent with maximum energies achievable in compact, strongly magnetized regions of parsec-scale jets, where the Larmor radius of accelerated protons remains smaller than the size of the emitting region. The electron-to-proton energy ratios $K_{\text{ep}} = 0.44$ for LEDA 55267 and $K_{\text{ep}} = 0.54$ for LEDA 58287 indicate that protons carry a substantial fraction of the total particle energy, with the total non-thermal energy budget implied by these fits remaining within the range expected for FR0 jets given their radio luminosities of $10^{38.69}$ and $10^{39.15}$ erg s $^{-1}$ (Baldi et al. 2018), and consistent with the jet powers inferred from the simulation setup described in Section 3.1. This suggests that the lepto-hadronic scenario does not require energetically extreme conditions and is physically compatible with typical FR0 systems.

The recollimation shocks identified in our RHD simulations, discussed in Section 4.1, are efficient particle acceleration sites where both electrons and protons can be energized via diffusive shock acceleration (Blandford & Eichler 1987; Kowal et al. 2011; de Gouveia Dal Pino & Kowal 2015; Kagan et al. 2015). The compact, parsec-scale emitting regions inferred from the SED fits are consistent with the strongly magnetized conditions required for proton confinement and acceleration to TeV–PeV energies (Boula et al. 2025). Moreover, FR0 sources are the most numerous jetted AGN population in the local Universe (Baldi et al. 2018), and even a modest individual contribution to the diffuse cosmic-ray and neutrino backgrounds could be collectively significant (Tavecchio et al. 2018; Merten et al. 2021; Lundquist et al. 2025).

To determine which model provides the best statistical description of the data, we adopt the Bayesian Information Criterion (BIC; Kass & Raftery 1995; Szydlowski et al. 2015; Trotta 2008). The evidence in favor of model i over model j is quantified through the log Bayes factor $|\ln B_{ij}| = -(\text{BIC}_i - \text{BIC}_j)/2$, interpreted according to the following scale: inconclusive if $|\ln B_{ij}| \leq 1.0$, weak evidence if $1.0 < |\ln B_{ij}| \leq 2.5$, moderate evidence if $2.5 < |\ln B_{ij}| \leq 5.0$, and strong evidence if $|\ln B_{ij}| > 5.0$. For LEDA 55267, the leptonic and lepto-hadronic fits including CTAO prospects yield $\text{BIC} = 5691.13$ and $\text{BIC} = 4814.84$, respectively, giving $|\ln B_{ij}| = 438.15$. For LEDA 58287, the corresponding values are $\text{BIC} = 3439.98$ and $\text{BIC} = 2506.30$, giving $|\ln B_{ij}| = 466.84$. In both cases, the evidence strongly favors the lepto-hadronic scenario when the simulated CTAO prospects are included. This conclusion is further supported by the model weights proposed by Burnham & Anderson (2002). Defining $\Delta_i = \text{BIC}_i - \text{BIC}_{\text{min}}$, the weight of model i is

$$w_i = \frac{\exp(-\frac{1}{2}\Delta_i)}{\sum_{r=1}^R \exp(-\frac{1}{2}\Delta_r)}, \quad (16)$$

which assigns a probability of 100% to the lepto-hadronic model for both sources when the CTAO prospects are incorporated.

We stress once more that this preference does not arise from the currently available data, but it emerges only when the simulated TeV flux points are included, and should therefore be interpreted as a theoretical prediction to be tested by future CTAO observations. At GeV energies, leptonic and lepto-hadronic models produce degenerate predictions, since the hadronic component contributes negligibly below ~ 1 TeV. It is precisely in the TeV regime that the two scenarios diverge, with the hadronic pion-decay emission rising steeply and dominating the total flux, as clearly visible in the bottom panels of Figure 6. This degeneracy at GeV energies and divergence at TeV energies is a well-known challenge in AGN jet modeling (Böttcher et al. 2013) and underscores the unique diag-

Table 5. Best-fit parameters of the leptonic, leptonic with CTAO prospects, and lepto-hadronic with CTAO prospects models for LEDA 55267 and LEDA 58287. Dashes indicate parameters not applicable to the corresponding scenario. K_{ep} is the ratio of the total energy in relativistic electrons to that in relativistic protons.

| Parameter | Leptonic | Leptonic+CTAO | Lepto-hadronic+CTAO |
|--------------------------|-----------------------|-----------------------|-----------------------|
| <i>LEDA 55267</i> | | | |
| p_e | 2.72 | 1.84 | 2.55 |
| $E_{\text{cut,e}}$ [TeV] | 0.21 | 3.12 | 0.25 |
| B [G] | 1.75×10^{-2} | 1.00×10^{-2} | 1.06×10^{-2} |
| R [cm] | 3.51×10^{18} | 1.00×10^{17} | 4.46×10^{18} |
| p_p | — | — | 0.01 |
| $E_{\text{cut,p}}$ [TeV] | — | — | 3.78 |
| K_{ep} | — | — | 0.44 |
| <i>LEDA 58287</i> | | | |
| p_e | 2.42 | 2.17 | 2.34 |
| $E_{\text{cut,e}}$ [TeV] | 0.31 | 2.56 | 0.12 |
| B [G] | 2.56×10^{-3} | 1.00×10^{-2} | 1.06×10^{-2} |
| R [cm] | 8.25×10^{18} | 1.00×10^{17} | 8.60×10^{18} |
| p_p | — | — | 0.01 |
| $E_{\text{cut,p}}$ [TeV] | — | — | 2.86 |
| K_{ep} | — | — | 0.54 |

nostic power of the CTAO. Future observations of approximately 200 hours with the CTAO North array at a zenith angle of 20° will be essential to discriminate between these scenarios and to establish whether FR0 radio galaxies are genuine sites of hadronic particle acceleration and significant contributors to the diffuse high-energy neutrino and cosmic-ray backgrounds. We note that this observation time represents a conservative reference rather than a sufficient threshold, since as shown in Figure 6, 200 hours are not enough to detect significant flux points in the leptonic scenario nor to fully resolve the lepto-hadronic component at the lowest TeV energies, reflecting the intrinsic faintness of FR0 sources compared to the classical AGN targets of Cherenkov observatories. This reference nevertheless illustrates the potential contribution of the CTAO to FR0 science and motivates future studies of how detection significance scales with observation time for sources of this luminosity class.

4.4 Plasma magnetization and β_p estimates

The synthetic emission maps presented in Section 4.2 identified the central regions of the jet, where recollimation shocks and turbulent mixing are most active, as the primary sites of synchrotron and inverse Compton emission. To assess the consistency between the jet simulations and the leptonic emission scenario, we estimate the magnetic field strength by relating it to the thermal pressure of the simulated flow. Although the magnetic field is not evolved self-consistently in the RHD simulations, this approach provides an order-of-magnitude estimate widely adopted in the literature when direct observational constraints on the field geometry are unavailable (Wilson & Scheuer 1983; Gomez et al. 1995; Seo et al. 2023; de Oliveira et al. 2025). Under the assumption that the simulation pressure corresponds to the thermal pressure, the magnetic field strength is estimated through the plasma beta parameter

$$\beta_p = \frac{P}{P_B} = \frac{8\pi P}{B^2}, \quad (17)$$

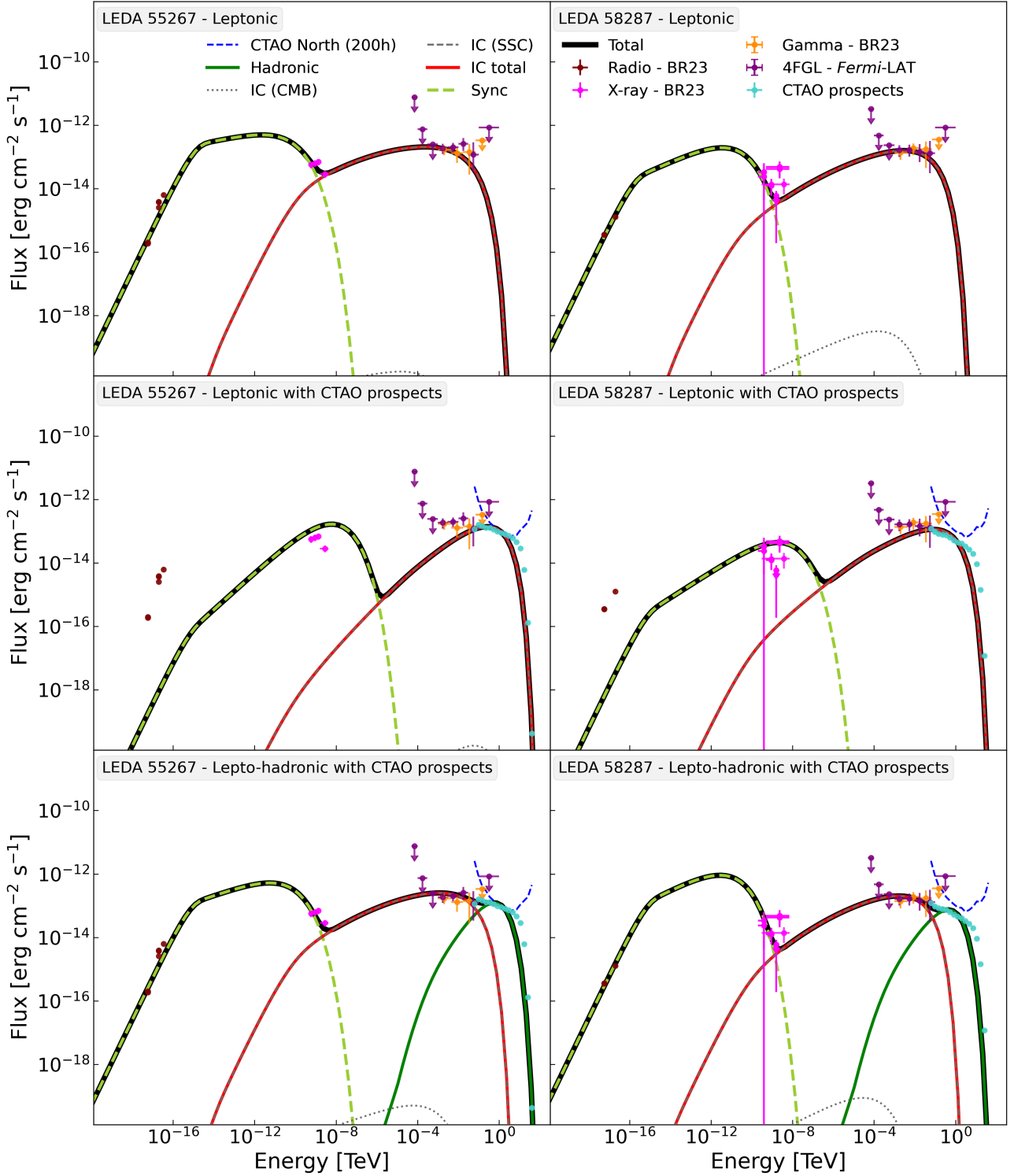


Figure 6. Broadband SED models for LEDA 55267 (left panels) and LEDA 58287 (right panels). From top to bottom, the panels show the leptonic model, the leptonic model with CTAO prospects, and the lepto-hadronic model with CTAO prospects. Data points: brown, magenta, and orange correspond to radio, X-ray, and gamma-ray measurements from BR23, respectively; purple to gamma-ray flux points from the 4FGL *Fermi*-LAT catalog (Abdollahi et al. 2020; Ballet et al. 2023); and light-blue to simulated CTAO flux points. Curves: blue dashed, CTAO sensitivity; green solid, hadronic flux contribution; gray dotted, inverse Compton emission from the CMB; gray dashed, synchrotron self-Compton emission from the emitting region; red solid, total inverse Compton emission; olive dashed, synchrotron emission; black solid, total emission.

where $P_B = B^2/8\pi$ is the magnetic pressure, so that

$$B = \sqrt{\frac{8\pi P}{\beta_p}}. \quad (18)$$

We perform a leptonic analysis using NAIMA (Zabalza 2015), adopting the best-fit parameters from Table 5 for all quantities except the magnetic field, which is determined by Equation 18 for a range of β_p values. The value of β_p that best reproduces the observed SED is identified by visual comparison with the direct NAIMA fit, and the results are shown in Figure 7.

For LEDA 55267, the best-fitting magnetic field $B = 1.75 \times 10^{-2}$ G yields $\beta_p = 2.0 \times 10^{-5}$, while for LEDA 58287, $B = 2.56 \times 10^{-3}$ G gives $\beta_p = 1.0 \times 10^{-3}$. In both cases, the red curve in Figure 7 reproduces the direct NAIMA fit very closely, confirming the internal consistency of the approach.

The inferred values of β_p are several orders of magnitude smaller than unity for both sources, indicating that the magnetic pressure strongly dominates over the thermal pressure in the emitting regions. This regime, often referred to as magnetically dominated or high-magnetization ($\sigma \gg 1$), is physically distinct from what is typically observed in extended FRI jets. For comparison, de Oliveira et al. (2025) report β_p values in the range 50–810 for regions of FRI jets with magnetic field strengths of 30–80 μ G. The much smaller values obtained here reflect the significantly stronger magnetic fields characteristic of the compact, parsec-scale emitting regions of LEDA 55267 and LEDA 58287 (Baldi et al. 2019; Giovannini et al. 2023), and indicate that these sources operate in a magnetically dominated regime fundamentally different from that of classical FRI jets.

The very small values of β_p inferred here have a direct counterpart at the level of the relativistic particle population. While β_p compares the magnetic to the thermal pressure, a more complete characterization of the magnetization of the emitting region is provided by the ratio $u_B/(u_e + u_p)$, where $u_B = B^2/8\pi$ and u_e , u_p are the energy densities of the relativistic electrons and protons inferred from the SED fits. Using the lepto-hadronic best-fit parameters listed in Table 5, in particular $B = 1.06 \times 10^{-2}$ G for both sources, $K_{ep} = 0.44$ for LEDA 55267 and $K_{ep} = 0.54$ for LEDA 58287, together with the ECPL spectra and TeV-scale cutoffs, we obtain $u_B/(u_e + u_p) \gg 1$ for both sources. This contrasts with the equipartition or particle-dominated regime ($u_B/(u_e + u_p) \ll 1$) typically reported on kiloparsec scales in extended FRI jets (Khataiya et al. 2024; de Oliveira et al. 2025). The contrast reflects the compactness of FR0 jets, as FRI flows propagate over kiloparsec scales and gradually convert magnetic energy into particle kinetic energy, whereas FR0 jets are disrupted within a few tens of parsecs by the recollimation instabilities described in Section 4.1, before significant magnetic-to-kinetic energy conversion can take place.

The physical origin of such low β_p values in FR0 jets can be understood in terms of their compactness and the conditions near the jet base. In the framework of magnetically arrested disc (MAD) accretion and Blandford–Znajek jet launching (Blandford & Znajek 1977; Tchekhovskoy & McKinney 2012), the jet is expected to emerge in a strongly magnetized state with $\beta_p \ll 1$ at parsec scales, before magnetic energy is gradually dissipated into particle kinetic energy at larger distances. FR0 jets, which are disrupted on scales of less than a few tens of parsecs by the recollimation instabilities described in Section 4.1, may therefore retain a high degree of magnetization that is already dissipated in the more extended FRI and FRII jets (Boula et al. 2025). This interpretation is consistent with the RMHD simulations of Boula et al. (2025), which find that magnetic fields play a stabilizing role in FR0 jets and can suppress or delay the develop-

ment of the same recollimation instabilities identified in our purely hydrodynamical simulations.

In a magnetically dominated regime, the magnetic field acts as the primary agent of particle acceleration and cooling. Processes such as magnetic reconnection, which become efficient when $\sigma \gg 1$, can accelerate both electrons and protons to very high energies through non-thermal power-law distributions (Sironi & Spitkovsky 2014; Werner et al. 2018), consistent with the exponential cutoff power-law spectra adopted in our SED modeling. The short cooling timescales associated with strong magnetic fields also naturally explain the compact extent of the emitting regions inferred from the SED fits in Table 5. Taken together, the small β_p values inferred from both sources indicate that FR0 jets operate in a physical regime fundamentally different from that of classical FRI sources, and that magnetic effects are central to understanding their dynamics, morphology, and high-energy emission.

It is important to note that the simulations presented in this work do not include magnetic fields dynamically, following the RHD framework established by Costa et al. (2024). While Boula et al. (2025) have already explored the RMHD regime for FR0 jets with a focus on jet stability and the role of magnetic fields in the recollimation process, here we connect the jet dynamics to the broadband high-energy emission through SED modeling and CTAO prospects. The very low β_p values inferred from the leptonic analysis suggest that magnetic fields may play a dynamically relevant role in the stability and collimation of these jets, providing strong motivation for future simulations in the RMHD regime, in which the magnetic field is evolved self-consistently and its dynamical role in jet stability, collimation, and energy dissipation can be directly assessed in conjunction with lepto-hadronic radiative modeling.

5 DISCUSSION AND CONCLUSIONS

We investigated the nature of compact jets in FR0 radio galaxies by combining three-dimensional RHD simulations with broadband SED modeling from radio to TeV energies. Our study focused on LEDA 55267 and LEDA 58287, both associated with GeV gamma-ray emission, with the aim of understanding the physical mechanisms governing jet disruption and assessing their detectability with the CTAO. The main results are summarized as follows.

The RHD simulations show that light, moderately relativistic jets propagating through an external medium develop strong recollimation shocks that trigger hydrodynamical instabilities, breaking the jet axisymmetry and driving the flow into a highly turbulent regime. These instabilities promote efficient mixing between the jet and the ambient medium, leading to rapid energy dissipation and deceleration that prevent the jet from expanding beyond a few tens of parsecs. This scenario provides a physically consistent explanation for the compact morphology observed in FR0 radio galaxies (Giovannini et al. 2023), and is in qualitative agreement with independent RHD and HD simulations of FR0 jets (Costa et al. 2024, 2026; Borodina et al. 2025). Synthetic synchrotron and inverse Compton emission maps derived from the simulations reproduce the main morphological features of the observed radio maps, with the emission concentrated in the central regions where jet–ambient medium interaction is most intense. In the broader context of FR0 studies, our results support the scenario in which these sources host intrinsically compact and efficiently disrupted jets, in line with the picture consolidated by recent reviews (Baldi 2023).

The external medium pressure and density are based on values inferred for M87 and consistent with the range observed in early-

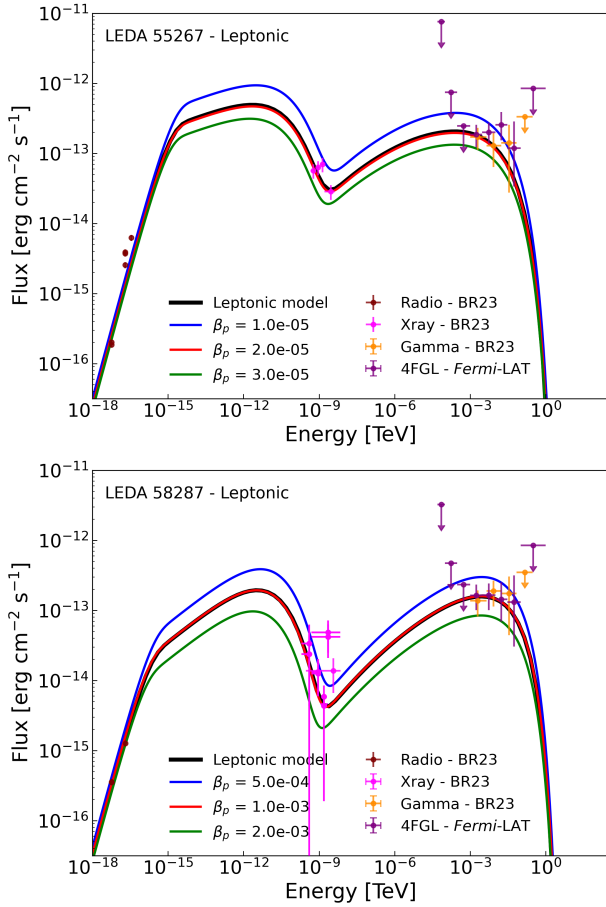


Figure 7. Leptonic model fits for LEDA 55267 (upper panel) and LEDA 58287 (lower panel) for different values of the plasma parameter β_p . In each panel, the black curve corresponds to the reference leptonic model with the parameters listed in Table 5, while the blue, red, and green curves show the fits obtained for varying β_p . For LEDA 55267, the three curves correspond to $\beta_p = 1.0 \times 10^{-5}$, 2.0×10^{-5} , and 3.0×10^{-5} , respectively, with the red curve ($\beta_p = 2.0 \times 10^{-5}$) providing the best agreement with the data. For LEDA 58287, the curves correspond to $\beta_p = 4.0 \times 10^{-4}$, 1.0×10^{-3} , and 2.0×10^{-3} , respectively, with the red curve ($\beta_p = 1.0 \times 10^{-3}$) providing the best agreement.

type galaxies at low redshift, as discussed in Section 3.1. As shown by Costa et al. (2024), the disruption behavior is not sensitive to moderate variations in the external medium profile, provided that the power-law index satisfies $\eta < 2$, which is well within the range expected for the interstellar medium of early-type host galaxies. Similarly, the choice of jet density contrast and initial velocity is consistent with the observational constraints available for FRO jets (Baldi et al. 2019; Giovannini et al. 2023), and the qualitative agreement between our results and those of independent simulations using different parameter choices suggests that the recollimation instability mechanism is a general feature of light, moderately relativistic jets in this class of sources rather than an artifact of our specific setup. Nevertheless, a systematic parameter study exploring the full range of FRO jet and environment properties would be valuable to quantify the conditions under which disruption is inevitable and to establish whether the mechanism operates across the entire FRO population.

The broadband SED modeling, performed with the *NATMA* package and incorporating the most recent 4FGL *Fermi*-LAT data (Abdollahi et al. 2020; Ballet et al. 2023), indicates that purely leptonic scenarios

adequately reproduce the observed emission up to GeV energies, with best-fit magnetic field strengths of 0.002–0.02 G in agreement with Khatiya et al. (2024) and Merten et al. (2021). However, when simulated CTAO flux points are included, leptonic models struggle to account for the TeV emission alongside the GeV data, whereas lepto-hadronic scenarios provide a significantly better description of the full energy range. We note that the lepto-hadronic fits show some tension at energies of the order of ~ 1 TeV, where the transition between the leptonic and hadronic components is not fully captured by the current modeling framework. This energy range corresponds to the regime where inverse Compton and pion-decay contributions overlap and where the CTAO sensitivity curve begins to constrain the simulated flux points. A more detailed treatment of this transition, potentially including additional radiative processes such as proton synchrotron emission or cascades, may be required to fully reproduce the spectral shape in this intermediate regime, and represents a natural direction for future work. Statistical model comparison based on the BIC yields $|\ln B_{ij}| = 438.15$ for LEDA 55267 and $|\ln B_{ij}| = 466.84$ for LEDA 58287, both firmly in the strong-evidence regime in favor of the lepto-hadronic scenario. The Burnham–Anderson model weights assign 100% probability to the lepto-hadronic model for both sources when the CTAO prospects are considered. This preference reflects the well-known degeneracy between leptonic and lepto-hadronic models at GeV energies and their divergence at TeV energies (Böttcher et al. 2013), underscoring the unique diagnostic power of the CTAO. Approximately 200 hours of observation with the CTAO North array at a zenith angle of 20° will be required to begin probing the TeV regime for these sources, and such detections would provide decisive constraints on the particle composition and acceleration processes operating in compact FRO jets.

The leptonic analysis of the jet simulations, based on the relationship between thermal pressure and magnetic field strength through the plasma parameter β_p , reveals that the emitting regions of both sources are strongly magnetized, with $\beta_p = 2.0 \times 10^{-5}$ for LEDA 55267 and $\beta_p = 1.0 \times 10^{-3}$ for LEDA 58287. These values are orders of magnitude smaller than those reported for extended FRI jets (de Oliveira et al. 2025), indicating that magnetic pressure strongly dominates over thermal pressure in the compact emitting regions of FRO sources. We note that Figure 7 reveals a degree of degeneracy in the β_p values consistent with the observed SED, in the sense that a range of β_p values produces acceptable fits within the current data uncertainties. This degeneracy reflects the limited ability of the present multiwavelength dataset to independently constrain both the magnetic field strength and the emitting region size simultaneously, and indicates that the inferred β_p values should be interpreted as order-of-magnitude estimates rather than precise measurements. Future observations extending the spectral coverage, particularly at X-ray and TeV energies, would help break this degeneracy and provide tighter constraints on the magnetization state of FRO jets.

The high magnetization inferred for FRO jets can be understood in the framework of magnetically arrested disc accretion and Blandford–Znajek jet launching (Blandford & Znajek 1977; Tchekhovskoy & McKinney 2012), in which jets emerge strongly magnetized near the base and gradually dissipate magnetic energy as they propagate outward. Unlike FRI and FRII sources, whose jets extend to kiloparsec scales where this dissipation is substantial, FRO jets are disrupted within a few tens of parsecs and therefore retain the high magnetization inherited from the launching region, providing a natural physical link to the lepto-hadronic emission preferred by our SED modeling. This interpretation is supported by Boula et al. (2025) and consistent with parsec-scale synchrotron observations (Baldi et al. 2019; Giovannini et al. 2023). The omission of

magnetic stresses in our RHD simulations implies that our results represent a lower-limit scenario for jet stability, and incorporating magnetic pressure in future simulations will be essential to assess the robustness of the conclusions presented here.

The simulations adopted in this work assume a light jet with density contrast $\rho_j/\rho_{\text{ext}} \approx 10^{-4}$, motivated by the standard picture of relativistic AGN jets emerging from low-density, magnetically dominated regions near the central engine, and consistent with the prescription of [Costa et al. \(2024\)](#). A hadronic-heavy jet, with a larger proton content and therefore larger rest-mass density and inertia, would be substantially less sensitive to the recollimation instabilities that drive the disruption seen in our runs, since the higher momentum flux $\rho h\Gamma^2 v^2$ would make it more difficult for ambient pressure imbalances to deflect and destabilize the beam, allowing the flow to maintain a coherent, axisymmetric structure over significantly larger distances. As a direct consequence, such a jet would penetrate deeper into the ambient medium before being decelerated by mass loading, producing a more extended morphology that approaches FRI rather than FR0 structures and no longer reproduces the sub-kpc termination observed in LEDA 55267 and LEDA 58287. The mixing dynamics would also differ, because in the light-jet runs the density contrast between jet and ambient material drops rapidly as the instabilities entrain external gas (Figure 2c), whereas a hadronic-heavy flow would carry a comparable rest-mass density of its own, reducing the relative impact of entrainment and the efficiency of energy dissipation through turbulent mixing. Finally, although a larger proton content could in principle enhance hadronic processes such as proton-proton and proton- γ interactions, the broader spatial extent and the more efficient dissipation of magnetic energy expected for a heavier jet would tend to lower the magnetization of the emitting region, weakening the confinement of accelerated protons and reducing the maximum energies achievable in the diffusive shock acceleration scenario. This would be in apparent tension rather than in agreement with the lepto-hadronic preference inferred from our SED analysis (Section 4.3) and with the very low β_p values discussed in Section 4.4.

The compact, sub-kpc morphology and the strongly magnetized emitting regions of FR0s are therefore most naturally reproduced by light jets undergoing rapid recollimation-driven disruption, and a quantitative exploration of hadronic-heavy configurations within the RMHD framework, where magnetic stresses can interact non-trivially with a proton-loaded flow, is left to future work.

Taken together, our results indicate that FR0 radio galaxies are not simply less powerful versions of FRIs, but constitute a physically distinct class of jetted AGN whose compact, unstable, and strongly magnetized jets can act as efficient accelerators of high-energy particles. The compactness of FR0 jets is not a consequence of lower power alone, but reflects an early disruption driven by recollimation instabilities that preserves the high magnetization inherited from the jet launching region. Given that FR0s are the most numerous jetted AGN population in the local Universe ([Baldi et al. 2018](#)), their collective contribution to the diffuse cosmic-ray and neutrino backgrounds may be significant ([Merten et al. 2021](#); [Lundquist et al. 2025](#)), and future CTAO detections will be essential to establish their role in the context of high-energy astrophysics.

The low β_p values inferred from the leptonic analysis suggest that magnetic fields may play a dynamically relevant role in the stability and collimation of FR0 jets, and that the turbulent structures identified in our simulations may favor the development of magnetic reconnection events capable of efficiently producing the high-energy non-thermal emission observed in these sources. Future investigations combining RMHD simulations with lepto-hadronic radiative models and CTAO observations ([Cherenkov Telescope Array Consortium](#)

[et al. 2018](#)) will be essential to establish more robust connections between jet plasma dynamics, particle acceleration mechanisms, and the observed gamma-ray emission in FR0 radio galaxies.

ACKNOWLEDGEMENTS

We sincerely thank the referee for their thoughtful feedback and valuable suggestions, which have greatly enhanced the clarity and scientific rigor of this work. A.F.S. Cardoso acknowledges the scholarship from FAPES N° 14/2023 - PROCAP 2024 PhD. A.F.S. Cardoso acknowledges A. Costa for helpful discussions. R.C.A. acknowledges S. Boula, JS. Wang and B. Reville for fruitful discussions. R.C.A. acknowledges the financial support of the NAPI “Fenômenos Extremos do Universo” of Fundação de Apoio à Ciência, Tecnologia e Inovação do Paraná. R.C.A. research is supported by CAPES/Alexander von Humboldt Program (grant No. 88881.800216/2022-01), CNPq (grant No. 308859/2025-1), Araucária Foundation (grant Nos. 698/2022 and 721/2022) and FAPESP (grant No. 2021/01089-1). R.C.A. also acknowledges the support of L’Oreal Brazil, with the partnership of ABC and UNESCO in Brazil. The authors acknowledge the AWS Cloud Credit/CNPq and the National Laboratory for Scientific Computing (LNCC/MCTI, Brazil) for providing HPC resources of the SDumont supercomputer, which have contributed to the research results reported in this paper. URL: <https://sdumont.lncc.br>. The authors acknowledge the Laboratory of Computational Astrophysics of the Universidade Federal de Itajubá (LAC-UNIFEI). The LAC-UNIFEI is maintained with grants from CAPES, CNPq and FAPEMIG. The research also used Gammapy, a Python package developed by the community for TeV gamma-ray astronomy ([Deil et al. 2017b,a](#); [Donath et al. 2023](#)), accessible at <https://www.gammapy.org>.

DATA AVAILABILITY

The data supporting this study are available from the corresponding author upon reasonable request.

REFERENCES

- Abdo A. A., et al., 2009, *ApJ*, 707, 55
 Abdo A. A., et al., 2010, *Science*, 328, 725
 Abdollahi S., et al., 2020, *ApJS*, 247, 33
 Acero F., et al., 2015, *ApJS*, 218, 23
 Acero F., et al., 2025, Gammapy v1.3: Python toolbox for gamma-ray astronomy, doi:10.5281/zenodo.14760974, <https://doi.org/10.5281/zenodo.14760974>
 Aharonian F. A., Kelner S. R., Prosekin A. Y., 2010, *Phys. Rev. D*, 82, 043002
 Angioni R., et al., 2019, *A&A*, 627, A148
 Atayan A. M., Aharonian F. A., 1996, *MNRAS*, 278, 525
 Baldi R. D., 2023, *A&ARv*, 31, 3
 Baldi R. D., Capetti A., Giovannini G., 2015, *A&A*, 576, A38
 Baldi R. D., Capetti A., Massaro F., 2018, *A&A*, 609, A1
 Baldi R. D., Torresi E., Migliori G., Balmaverde B., 2019, *Galaxies*, 7, 76
 Baldi R. D., Giovannini G., Capetti A., Lico R., 2025, *arXiv e-prints*, p. [arXiv:2501.03787](https://arxiv.org/abs/2501.03787)
 Ballet J., Bruel P., Burnett T. H., Lott B., The Fermi-LAT collaboration 2023, *arXiv e-prints*, p. [arXiv:2307.12546](https://arxiv.org/abs/2307.12546)
 Blandford R., Eichler D., 1987, *Phys. Rep.*, 154, 1
 Blandford R. D., Znajek R. L., 1977, *MNRAS*, 179, 433
 Blandford R., Meier D., Readhead A., 2019, *ARA&A*, 57, 467
 Boizelle B. D., Li X., LeVar N., Norcross S., Derieg B. J., Davidson J. R., Siaw K., Walsh J. L., 2025, *ApJ*, 989, 83

- Borodina O., et al., 2025, *ApJ*, **981**, 149
- Boroson B., Kim D.-W., Fabbiano G., 2011, *ApJ*, **729**, 12
- Böttcher M., Reimer A., Sweeney K., Prakash A., 2013, *ApJ*, **768**, 54
- Boughelilba M., Reimer A., 2023, *ApJ*, **955**, L41
- Boula S., Tavecchio F., Bodo G., Vlahakis N., Coppi P., Costa A., Sciacaluga A., 2025, *A&A*, **704**, A200
- Bronzini E., et al., 2024a, *A&A*, **684**, A65
- Bronzini E., Grandi P., Torresi E., Buson S., 2024b, *ApJ*, **977**, L16
- Burnham K. P., Anderson D. R., 2002, Model Selection and Multimodel Inference, 2 edn. Springer, New York, doi:10.1007/b97636
- Buson S., Tramacere A., Pfeiffer L., Oswald L., de Menezes R., Azzollini A., Ajello M., 2022, *ApJ*, **933**, L43
- Canizares C. R., Fabbiano G., Trinchieri G., 1987, *ApJ*, **312**, 503
- Cao Z., et al., 2024, *ApJ*, **971**, L45
- Capetti A., Massaro F., Baldi R. D., 2017a, *A&A*, **598**, A49
- Capetti A., Massaro F., Baldi R. D., 2017b, *A&A*, **601**, A81
- Capetti A., Massaro F., Baldi R. D., 2020a, *A&A*, **633**, A161
- Capetti A., et al., 2020b, *A&A*, **642**, A107
- Cardoso A., Anjos R., 2026, in High Energy Phenomena in Relativistic Outflows IX (HEPRO-IX). p. 071, doi:10.22323/1.510.0071
- Cheng X.-P., An T., 2018, *ApJ*, **863**, 155
- Cheng X., An T., Sohn B. W., Hong X., Wang A., 2021, *MNRAS*, **506**, 1609
- Cherenkov Telescope Array Consortium et al., 2018, Science with the Cherenkov Telescope Array. WORLD SCIENTIFIC, doi:10.1142/10986, <http://dx.doi.org/10.1142/10986>
- Chilufya J., Hardcastle M. J., Pierce J. C. S., Croston J. H., Mingo B., Zheng X., Baldi R. D., Röttgering H. J. A., 2024, *MNRAS*, **529**, 1472
- Collaboration I., et al., 2018, *Science*, **361**, 147
- Collaboration*† I., et al., 2022, *Science*, **378**, 538
- Costa A., et al., 2024, *A&A*, **682**, L19
- Costa A., Bodo G., Tavecchio F., Rossi P., Coppi P., Sciacaluga A., Boula S., 2026, *A&A*, **705**, A74
- Dainotti M. G., Ostrowski M., Harris D., Siemiginowska A., Siejkowski H., 2012, *MNRAS*, **426**, 218
- Deil C., Donath A., Owen E., Terrier R., Bühler R., Armstrong T., 2017a, Gammapy: Python toolbox for gamma-ray astronomy, Astrophysics Source Code Library, record ascl:1711.014 (ascl:1711.014)
- Deil C., et al., 2017b, in 35th International Cosmic Ray Conference (ICRC2017). p. 766 (arXiv:1709.01751), doi:10.22323/1.301.0766
- Dermer C. D., Razzaque S., Finke J. D., Atayan A., 2009, *New Journal of Physics*, **11**, 065016
- Di Mauro M., Calore F., Donato F., Ajello M., Latronico L., 2014, *ApJ*, **780**, 161
- Donath A., et al., 2023, *A&A*, **678**, A157
- Fanaroff B. L., Riley J. M., 1974, *MNRAS*, **167**, 31P
- Fu W.-J., Zhang H.-M., Zhang J., Liang Y.-F., Yao S., Liang E.-W., 2022, *Research in Astronomy and Astrophysics*, **22**, 035005
- Garofalo D., Singh C. B., 2019, *ApJ*, **871**, 259
- Garofalo D., Evans D. A., Sambruna R. M., 2010, *MNRAS*, **406**, 975
- Garofalo D., Singh C. B., Harmon E., Williams M., Castillo L. R., 2024, *Journal of High Energy Astrophysics*, **42**, 21
- Ghisellini G., 2011, in Aharonian F. A., Hofmann W., Rieger F. M., eds, American Institute of Physics Conference Series Vol. 1381, 25th Texas Symposium on Relativistic Astrophysics (Texas 2010). AIP, pp 180–198 (arXiv:1104.0006), doi:10.1063/1.3635832
- Giovannini G., Baldi R. D., Capetti A., Giroletti M., Lico R., 2023, *A&A*, **672**, A104
- Gomez J. L., Marti J. M. A., Marscher A. P., Ibanez J. M. A., Marcaide J. M., 1995, *ApJ*, **449**, L19
- Grandi P., Capetti A., Baldi R. D., 2016, *MNRAS*, **457**, 2
- Harvey M., Rulten C. B., Chadwick P. M., 2020, *MNRAS*, **496**, 903
- Inoue Y., 2011, *ApJ*, **733**, 66
- Jiang X., Lei H., Huang H.-Y., Zhang W., Li Y.-J., Wei D.-M., 2026, arXiv e-prints, p. arXiv:2603.21110
- Kagan D., Sironi L., Cerutti B., Giannios D., 2015, *Space Sci. Rev.*, **191**, 545
- Kass R. E., Raftery A. E., 1995, *Journal of the American Statistical Association*, **90**, 773
- Khangulyan D., Aharonian F. A., Kelner S. R., 2014, *ApJ*, **783**, 100
- Khatiya N. S., Boughelilba M., Karwin C. M., McDaniel A., Zhao X., Ajello M., Reimer A., Hartmann D. H., 2024, *ApJ*, **971**, 84
- Kowal G., de Gouveia Dal Pino E. M., Lazarian A., 2011, *ApJ*, **735**, 102
- Lalakos A., Tchekhovskoy A., Bromberg O., Gottlieb O., Jacquemin-Ide J., Liska M., Zhang H., 2024, *ApJ*, **964**, 79
- Landau L. D., Lifshitz E. M., 1959, Fluid mechanics. Pergamon Press
- Lundquist J. P., et al., 2025, *ApJ*, **978**, 20
- Massaro F., Capetti A., Paggi A., Baldi R. D., Tramacere A., Pillitteri I., Campana R., 2020, *ApJ*, **900**, L34
- Merten L., et al., 2021, *Astroparticle Physics*, **128**, 102564
- Mignone A., Plewa T., Bodo G., 2005, *ApJS*, **160**, 199
- Mignone A., Bodo G., Massaglia S., Matsakos T., Tesileanu O., Zanni C., Ferrari A., 2007, *ApJS*, **170**, 228
- Nawaz M. A., Bicknell G. V., Wagner A. Y., Sutherland R. S., McNamara B. R., 2016, *MNRAS*, **458**, 802
- Observatory C. T. A., Consortium C. T. A., 2021, CTAO Instrument Response Functions - prod5 version v0.1, doi:10.5281/zenodo.5499840, <https://doi.org/10.5281/zenodo.5499840>
- Paliya V. S., 2021, *ApJ*, **918**, L39
- Pannikkote M., Paliya V. S., Saikia D. J., 2023, *ApJ*, **957**, 73
- Roy N., et al., 2021, *ApJ*, **922**, 230
- Rulten C. B., Brown A. M., Chadwick P. M., 2020, *MNRAS*, **492**, 4666
- Saldana-Lopez A., Domínguez A., Pérez-González P. G., Finke J., Ajello M., Primack J. R., Paliya V. S., Desai A., 2021, *Monthly Notices of the Royal Astronomical Society*, **507**, 5144
- Seo J., Ryu D., Kang H., 2023, *ApJ*, **944**, 199
- Sironi L., Spitkovsky A., 2014, *ApJ*, **783**, L21
- Sparks W. B., Biretta J. A., Macchetto F., 1996, *ApJ*, **473**, 254
- Stawarz L., Aharonian F., Kataoka J., Ostrowski M., Siemiginowska A., Sikora M., 2006, *MNRAS*, **370**, 981
- Stecker F. W., Shrader C. R., Malkan M. A., 2019, *ApJ*, **879**, 68
- Sutherland R. S., Bicknell G. V., 2007, *ApJS*, **173**, 37
- Szydlowski M., Krawiec A., Kurek A., Kamionka M., 2015, *European Physical Journal C*, **75**, 5
- Tavecchio F., Righi C., Capetti A., Grandi P., Ghisellini G., 2018, *MNRAS*, **475**, 5529
- Tchekhovskoy A., McKinney J. C., 2012, *MNRAS*, **423**, L55
- Torresi E., Grandi P., Capetti A., Baldi R. D., Giovannini G., 2018, *MNRAS*, **476**, 5535
- Torresi E., et al., 2022, in Memorie della Societa Astronomica Italiana. p. 81, doi:10.36116/MEMSAIT_93N2_3.2022.10
- Trotta R., 2008, *Contemporary Physics*, **49**, 71
- Urry C. M., Padovani P., 1995, *PASP*, **107**, 803
- Werner G. R., Uzdensky D. A., Begelman M. C., Cerutti B., Nalewajko K., 2018, *MNRAS*, **473**, 4840
- Wilson M. J., Scheuer P. A. G., 1983, *MNRAS*, **205**, 449
- Zabalza V., 2015, Proc. of International Cosmic Ray Conference 2015, p. 922
- de Gouveia Dal Pino E. M., Kowal G., 2015, in Lazarian A., de Gouveia Dal Pino E. M., Melioli C., eds, Astrophysics and Space Science Library Vol. 407, Magnetic Fields in Diffuse Media. p. 373 (arXiv:1302.4374), doi:10.1007/978-3-662-44625-6_13
- de Oliveira C., Matthews J. H., de Souza V., 2025, *MNRAS*, **539**, 3697

This paper has been typeset from a $\text{\TeX}/\text{\LaTeX}$ file prepared by the author.